nature communications

Article

https://doi.org/10.1038/s41467-026-73626-8

A universal scaling law for active diffusion in complex media

Received: 20 July 2025

Accepted: 14 May 2026

Published online: 30 May 2026

Check for updates

Qun Zhang[1,7], Yuxin Tian[1,7], Xue Zhang[1], Xiaoting Yu[1], Hongwei Zhu[2], Ning Zheng[1] ✉, Luhui Ning[3] ✉, Ran Ni[4] ✉, Mingcheng Yang[5,6] ✉ & Peng Liu[1] ✉

Understanding how active particles transport in structurally heterogeneous environments is a fundamental and challenging problem, with relevance to biological and synthetic microswimmers in tissues and porous media. Here, using granular experiments and computer simulations, we investigate the long-time diffusion of active tracers in quasi-two-dimensional heterogeneous media. We show that diffusion-structure relations established for passive systems fail to describe active transport across different activity levels. To resolve this, we formulate a modified diffusion-structure relation by incorporating the dimensionless persistence length $Q = v_d\tau_r/d_t$, which captures the activity-induced extension of the effective interaction range. The proposed relation yields a consistent collapse within both experimental and simulation datasets across active and passive tracers, diverse environmental structures, and propulsion mechanisms. Our results thus provide a universal predictive framework for transport in non-equilibrium heterogeneous systems.

Active matter systems consist of self-driven units that convert stored or environmental energy into mechanical motion, including self-propelled particles[1–5], contractile active systems such as actomyosin networks[6,7], breathing particles[8,9], and growing particles[10,11]. Biological entities include bacteria[12,13], protozoa[14,15], and spermatozoa[16,17], whose propulsion is powered by molecular motor-driven flagella or cilia[18,19]. Synthetic microswimmers, by contrast, are typically actuated by chemical reactions[20,21] or external fields such as light[22,23], electromagnetic[24,25], or acoustic stimuli[26,27]. Their long-time transport properties show promise in a wide range of applications, from targeted delivery of drugs, biomarkers, and contrast agents[28–30], to the design of smart materials and microdevices[31,32]. In idealized structureless environments, an isolated active particle exhibits persistent ballistic motion at short times and transitions to an enhanced diffusion at long times due to stochastic reorientation[33,34]. In two-dimensional systems, the corresponding long-time diffusion coefficient is given by the well-established relation $D_a^0 = D_t^0 + v_d^2\tau_r/2$, where D_t^0 denotes that of the passive counterpart, v_d the propulsion speed, and τ_r the rotational relaxation time[33,35]. This description applies to an isolated active particle and does not account for the role of environmental structures, which introduce a motility-dependent effective interaction range. In practice, however, active particles typically move through complex environments such as biological tissues, porous media, and microfluidic networks. Considerable efforts have therefore been devoted to elucidating active transport in both homogeneous and heterogeneous media[33,36–38].

Complex background structures are known to profoundly alter active dynamics, giving rise to phenomena such as subdiffusion and trapping[39,40], dynamic freezing[41,42], and chirality-dependent sorting[43,44]. These observations raise a fundamental question: how does the structure of complex environments govern active diffusion? For passive systems,

[1]School of Physics, Beijing Institute of Technology, Beijing, China. [2]School of Physical Science and Technology, Key Laboratory of Magnetism and Magnetic Materials for Higher Education in Inner Mongolia Autonomous Region, Baotou Teachers' College, Baotou, China. [3]Beijing Key Laboratory of Optical Detection Technology for Oil and Gas, China University of Petroleum-Beijing, Beijing, China. [4]School of Chemistry, Chemical Engineering and Biotechnology, Nanyang Technological University, 62 Nanyang Drive, Singapore, Singapore. [5]Beijing National Laboratory for Condensed Matter Physics and Laboratory of Soft Matter Physics, Institute of Physics, Chinese Academy of Sciences, Beijing, China. [6]School of Physical Sciences, University of Chinese Academy of Sciences, Beijing, China. [7]These authors contributed equally: Qun Zhang, Yuxin Tian. ✉e-mail: ningzheng@bit.edu.cn; lhningphy@cup.edu.cn; r.ni@ntu.edu.sg; mcyang@iphy.ac.cn; liupeng@bit.edu.cn

https://doi.org/10.1038/s41467-026-73626-8

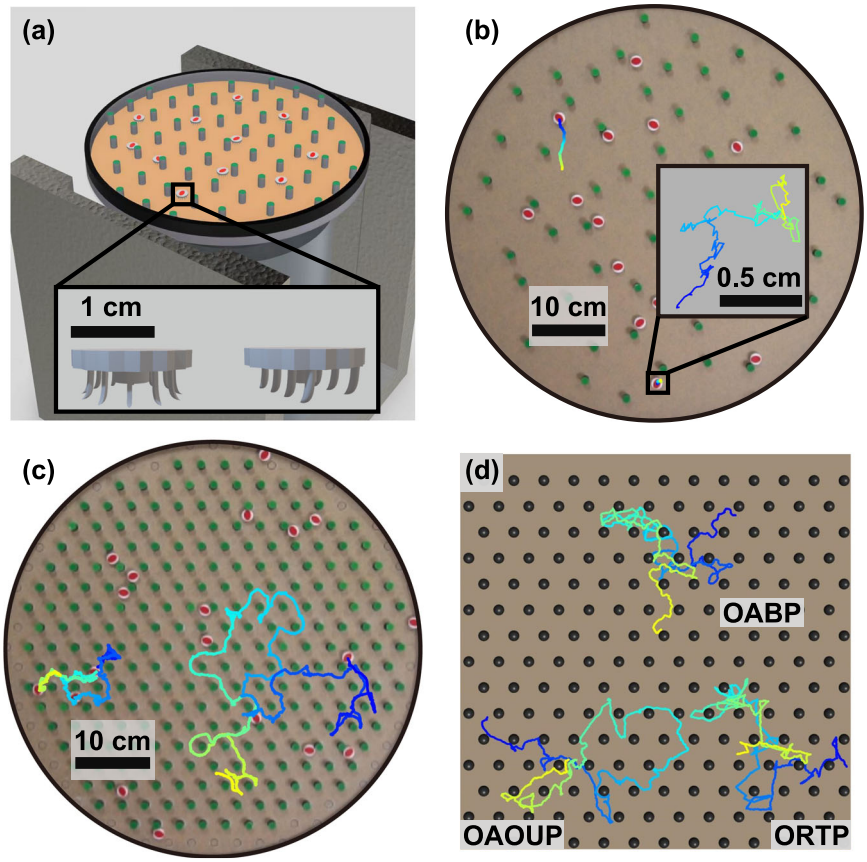

Fig. 1 | Experimental setup and tracer dynamics in complex environments. **a** Schematic of the quasi-2D electromagnetic shaker setup. The inset highlights 3D-printed tracer particles with symmetric (passive) and asymmetric (active) legs; propulsion speed v_d is tuned via the leg inclination angle. **b** Short-time trajectories (0–0.7 s) in a disordered background, where the upper path corresponds to an active tracer (v_d = 4.08 cm/s) and the lower path to a passive particle undergoing passive diffusion. **c** Long-time trajectories (0–70 s) in a hexagonal lattice: left, passive particle; right, active tracer (same as in (**b**)). **d** Simulated long-time trajectories of OABP, OAOUP, and ORTP tracers in a hexagonal lattice over 5×10^5 steps. In (**b**–**d**), trajectory color indicates time, from blue (start) to yellow (end).

extensive studies have established a universal diffusion-structure scaling that quantitatively links long-time normal diffusivity to the two-body structural entropy in both dynamic and quenched media[45–49]. With appropriate normalization, the diffusion coefficient D^* collapses over several orders of magnitude onto a single master curve, demonstrating robust universality across diverse environments. In contrast, analogous diffusion-structure relations for active systems remain largely unexplored, except for the recent simulation study on dense active glass formers[50]. Experimental investigations that directly link transport to structural properties in heterogeneous active systems are also lacking. Whether a unified diffusion-structure relation exists for active probes in external heterogeneous environments remains an open question.

In this work, combining granular experiments and particle-based simulations, we investigate the diffusion of active particles in various spatially heterogeneous environments, where obstacles are arranged in disordered structures as well as ordered square and hexagonal crystal lattices. We fabricate 3D-printed polylactide particles featuring tilted legs that allow the activity tuning via the inclination angle[51,52]. In simulations, self-propulsion is modeled using active Brownian motion[33,53], run-and-tumble dynamics[54,55], and active Ornstein-Uhlenbeck processes[56,57], both overdamped and underdamped. We show that diffusion-structure relations established for passive systems fail to collapse active transport across different activity levels in heterogeneous environments. By incorporating activity through a dimensionless persistence length Q, we recover a consistent collapse of the normalized diffusion coefficient D^*_{mod} as a function of the two-body structural entropy S_2[48,58], independent of the self-propulsion mechanism or the medium structure. This finding reveals a general active diffusion-structure relation and provides a predictive framework for long-time active diffusion in spatially heterogeneous environments.

Results

Experimental system and tracer dynamics

Disk-like tracers were placed in a 54-cm-diameter circular vessel mounted on an electromagnetic shaker [Fig. 1(a)]. As shown by the short-time [Fig. 1(b)] and long-time trajectories [Fig. 1(c)], passive tracers undergo random motion, whereas active tracers exhibit persistent directed motion at short times that gradually randomizes at longer times, consistent with the dynamics of persistent active Brownian motion [Supplementary Movies 1 and 2]. In simulations, active tracers are propelled with a speed v_d, leading to a long-time effective diffusivity $D_a^0 = D_t^0 + v_d^2\tau_r/2$ (measured in a free background without obstacles)[32], and reorient via three representative models: active Brownian particles (ABPs), run-and-tumble particles (RTPs), and active Ornstein-Uhlenbeck particles (AOUPs), which capture the stochastic dynamics of synthetic Janus colloids[33,53], *E. coli*-like swimmers[54,55], and particles driven by active baths[56,57], respectively. Each model was implemented in both overdamped and underdamped forms, labeled as OABP, ORTP, OAOUP and UABP, URTP, UAOUP, respectively. Representative long-time trajectories are shown in Fig. 1(d).

Diffusion and structural correlations

In both experiments and simulations, the long-time dynamics of active tracers are characterized by the diffusion coefficient D_a, extracted from the mean square displacements (MSDs) defined as $\langle \Delta \mathbf{r}^2(t) \rangle = \langle [\mathbf{r}(t_0 + t) - \mathbf{r}(t_0)]^2 \rangle$, where $\langle \cdot \rangle$ denotes the ensemble

https://doi.org/10.1038/s41467-026-73626-8

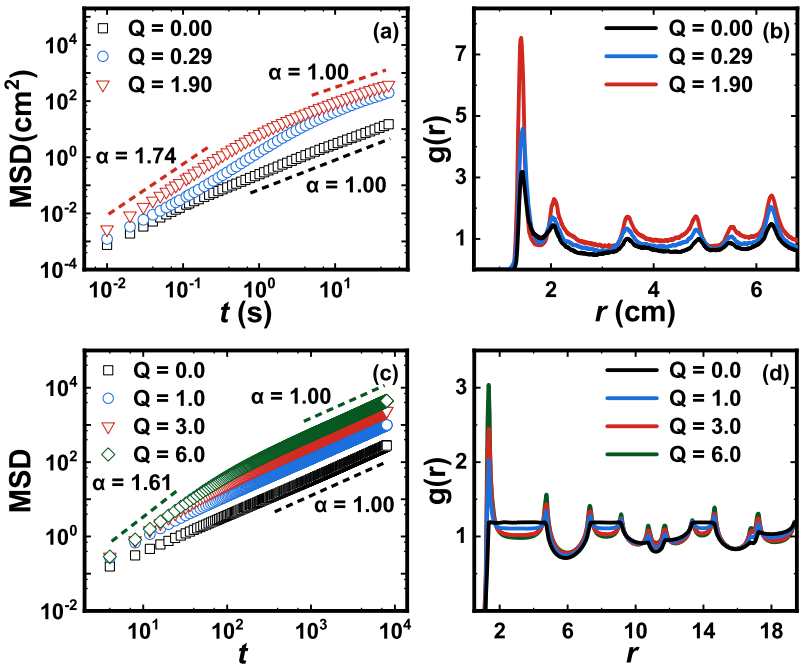

Fig. 2 | Diffusion and structural correlations of active tracers. a MSDs as a function of delay time t and (**b**) the pair correlation function $g(r)$ for passive ($Q = 0$) and active tracers with $Q = 0.29$ and 1.90, measured experimentally in a hexagonal lattice with lattice constant $L = 3$ cm and background packing fraction $\phi = 0.09$. Corresponding simulation results of (**c**) MSDs and (**d**) $g(r)$ for tracers with activity $Q = 0$, 1.0, 3.0 and 6.0 in a hexagonal lattice at $\phi = 0.10$. Source data are provided as a Source Data file.

average. Figure 2(a) shows log-log plots of MSDs for tracers with different activities, characterized by the Péclet-like parameter $Q = v_d\tau_r/d_t$ (with d_t the tracer diameter)[59], obtained experimentally in a hexagonal lattice with lattice constant $L = 3$ cm and background packing fraction $\phi = 0.09$. Passive tracers undergo normal diffusion ($\langle\Delta\mathbf{r}^2(t)\rangle \propto t^\alpha$, $\alpha = 1$), while active tracers exhibit a crossover from the short-time super-diffusion ($\alpha > 1$) to the long-time normal diffusion ($\alpha = 1$). The long-time diffusion coefficient D_a is extracted by fitting the MSDs with $\langle\Delta\mathbf{r}^2(t)\rangle = 4D_at$. Figure 2(c) presents simulated MSDs for tracers with different activities Q in a hexagonal lattice at slightly higher packing fraction $\phi = 0.10$, with D_a obtained using the same fitting procedure.

The structure of the system is characterized by the two-body structural entropy S_2, which approximates the excess entropy, *i.e.*, the entropy difference between a correlated system and an ideal gas under identical conditions. While the full excess entropy includes higher-order correlations, the two-body contribution S_2 accounts for more than 85% of the total excess entropy across a broad density range, and has been widely used as an approximation in complex systems[60]. For a tracer in a matrix, S_2 is computed from the pair correlation function $g(r)$ between the tracer and background particles[48,58]:

$$S_2 = -\pi\rho\int_0^\infty \{g(r)ln[g(r)] - [g(r)-1]\}rdr, \tag{1}$$

where ρ is the number density of background matrix particles. Given the low tracer concentration, tracer-tracer interactions are normally negligible, and only tracer-matrix correlations are considered. The function $g(r)$, defined as the probability of finding a matrix particle at distance r from a tracer, is measured by

$$g(r) = \frac{1}{2\pi r\rho}\left\langle \frac{1}{N_t}\sum_{i=1}^{N_t}\sum_{j=1}^{N_l}\delta(r - r_{ij})\right\rangle, \tag{2}$$

where N_t and N_l are the numbers of tracers and matrix particles, respectively, and r_{ij} is the distance between tracer i and matrix particle j. Experimentally measured $g(r)$ in a hexagonal lattice is shown in Fig. 2(b). As the activity Q increases from 0 (passive) to 1.90 (active), the first peak of $g(r)$, increases, indicating enhanced tracer-matrix correlations. The periodic peaks in $g(r)$, arising from the crystalline order of the matrix, are similarly observed in simulations across different Q [Fig. 2(d)]. In both experiments and simulations, the two-body structural entropy S_2 varies from sample to sample [Supplementary Note 1]. For disordered backgrounds, S_2 decreases with increasing obstacle number density ρ, whereas for crystalline backgrounds, S_2 depends on the lattice constant L. To sample a broad range of S_2, we prepare multiple backgrounds by tuning ρ in disordered backgrounds and varying L in square and hexagonal lattices.

Limits of diffusion-structure scaling

In the following, the long-time diffusion coefficients of both passive (D_t) and active (D_a) tracers are normalized as $D^* = D\Gamma^{-1}d_t^{-2}$, following the normalization widely used in previous studies[45,47–49]. The Enskog collision frequency Γ between the tracer and immobile matrix particles in 2D is given by refs. 48,61

$$\Gamma = 2r_p\rho g(r_p)\sqrt{\pi k_B T_{\text{eff}}/m}, \tag{3}$$

where r_p is the position of the first peak in $g(r)$ and m is the reduced mass, defined as $m = 2m_tm_l/(m_t + m_l)$, with m_t and m_l the masses of the tracer and background particles, respectively. Since matrix particles are fixed, they effectively form an infinite-mass rigid background, and we take the limit $m_l \to \infty$, yielding $m \approx 2m_t$. For passive tracers, the effective temperature T^p_{eff} is extracted from the average kinetic energy of tracers in the obstacle-free vibrated system[62,63]. For active tracers, it is defined as $k_BT^a_{\text{eff}} = k_BT^p_{\text{eff}}(D^0_a/D^0_t)$, accounting for their enhanced long-time diffusivity under identical translational damping, where both D^0_a and D^0_t are measured in the same obstacle-free background.

Figure 3 (a) plots the normalized diffusion coefficients D^* as a function of the two-body structural entropy S_2 for tracers with varying activity in disordered and ordered backgrounds. The experimental data do not collapse onto a single curve; instead, each activity level

https://doi.org/10.1038/s41467-026-73626-8

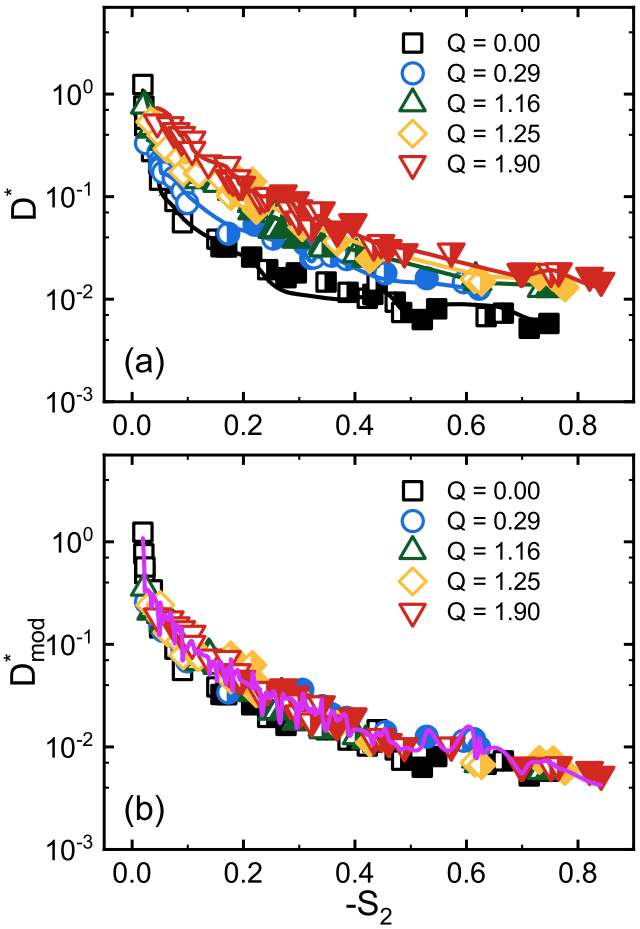

Fig. 3 | Breakdown and recovery of diffusion-structure scaling in experiments. **a** Experimentally measured dimensionless diffusion coefficient $D^* = D\Gamma^{-1}d_t^{-2}$ plotted against the two-body structural entropy S_2 for passive and active tracers with different activities Q in disordered and ordered backgrounds. Solid lines represent fits to the original scaling relation of Eq. (4). **b** The same data replotted using the activity-modified normalized $D^*_{mod} = D\left[\Gamma(1+Q)d_t^2\right]^{-1}$. All data collapse onto a single master curve, with the solid violet line representing the fit to Eq. (5), demonstrating a unified scaling behavior across both passive and active tracers. Open, half-filled, and solid symbols correspond to disordered, square-lattice, and hexagonal-lattice backgrounds, respectively. Source data are provided as a Source Data file.

follows its own trend. Moreover, the data at all activity levels deviate significantly from the Dzugutov-like scaling[45,50], $D^* = \beta e^{\alpha S_2}$, with β and α being fitting parameters. Particularly in the regime of small $-S_2$ where structural correlations are weak, pronounced discrepancies between the experimental results and the Dzugutov-scaling are observed [Supplementary Note 2], indicating that the empirical exponential form becomes inadequate as it does not explicitly account for the underlying binary collisional dynamics.

To elucidate the origin of these deviations, we decomposed the total friction experienced by the active tracer into three contributions: the effective Brownian friction ξ_S arising from the substrate, binary collisional friction ξ_B, and structural friction from local constraints $\xi_{\rho\rho}$. The long-time diffusion coefficient can then be expressed as $D = k_B T_{eff}/(\xi_S + \xi_B + \xi_{\rho\rho})$. Following the previously established dynamics-structure scaling relation, normalization by Γd_t^2 yields the scaling form[48,49]

$$D^* = \frac{k_B T_{\text{eff}}}{\Gamma d_t^2 \xi_B} \frac{1}{A(1-S_2) + \xi_S/\xi_B}, \tag{4}$$

where $\xi_B = 2r_p \rho g(r_p)\sqrt{\pi k_B T_{\text{eff}} m}$[64,65], and A is a fitting parameter. Since active and passive tracers interact with the same substrate and have nearly identical contact areas, the substrate friction coefficient, ξ_S, is assumed to be identical for both. It is obtained from the Einstein relation for passive diffusion in the absence of obstacles, $\xi_S = k_B T^p_{\text{eff}}/D_t^0$, an assumption commonly adopted in granular systems[66,67]. Interestingly, each activity level follows its own dynamics-structure scaling described by Eq. (4), demonstrating that long-time diffusivity is largely controlled by the two-body structural entropy S_2 of the environment. However, D^* systematically increases with tracer activity even at fixed S_2, and fitting Eq. (4) requires activity-dependent values for the fitting parameter A. This suggests that although the underlying coupling between structural entropy and long-time dynamics persists in active systems and Eq. (4) remains valid within subsets of fixed activity, it fails to quantitatively capture the universal nature of nonequilibrium dynamics.

Diffusion-structure scaling with persistence

In particular, the tracer diameter d_t reflects only the tracer's geometric size but neglects the directional persistence unique to active motion. Unlike passive tracers, active particles typically travel a distance $v_d\tau_r$ before reorientation, which effectively extends their interaction range along the propulsion direction from d_t to $d_t + v_d\tau_r$, thereby increasing the effective interaction area from d_t^2 to $(d_t + v_d\tau_r)d_t$. To quantify this persistence effect, we introduce the dimensionless persistence length $Q = v_d\tau_r/d_t$, a Péclet-like activity parameter widely used in active systems[59], which increases with both propulsion velocity and reorientation time. This parameter captures the directional memory associated with persistent self-propulsion, enhancing tracer-obstacle coupling beyond purely thermal models. Incorporating this activity-induced length scale, we define a modified dimensionless diffusion coefficient, $D^*_{mod} = D\left[\Gamma(1+Q)d_t^2\right]^{-1}$, which smoothly recovers the passive limit as $Q = 0$. Substituting this into Eq. (4) leads to the generalized scaling form:

$$D^*_{\text{mod}} = \frac{k_B T_{\text{eff}}}{\Gamma(1+Q)d_t^2 \xi_B} \frac{1}{A(1-S_2) + \xi_S/\xi_B}. \tag{5}$$

The self-propulsion speed v_d is extracted from particle trajectories, and the rotational relaxation time τ_r is obtained from $D_a^0 = D_t^0 + v_d^2\tau_r/2$, using the long-time diffusion coefficient of the active (D_a^0) and corresponding passive (D_t^0) tracers in the absence of obstacles[32] [Supplementary Note 3]. As shown in Fig. 3(b), all experimental data—spanning varying propulsion speeds and matrix structures—collapse onto a single master curve, in quantitative agreement with the modified diffusion-structure relation Eq. (5) with a single fitting parameter $A = 1$. This indicates that the relation properly captures the underlying physical mechanism rather than merely reflecting a case-specific fitting, and D^*_{mod} is entirely determined by S_2 and Q, with no discontinuities observed across the transition from passive to active diffusion. This establishes a unified scaling framework for long-time diffusion in heterogeneous media, bridging equilibrium and nonequilibrium systems via two experimentally accessible parameters.

Universality across active-particle models

Next, we further test the universality of the scaling relation through simulations of active colloidal tracers with diverse reorientation dynamics. Three representative models—ABP, AOUP, and RTP—are considered, each implemented under both underdamped and overdamped conditions to assess the effect of inertia. Figure 4(a) plots the dimensionless diffusion coefficient D^* as a function of S_2 for passive and active tracers in the UABP model. Like in Fig. 3(a), data points with different activities remain dispersed and do not collapse onto a single curve. Each trend is described by the original scaling relation Eq. (4), with an activity-dependent fitting parameter A. Passive tracers, shown in black, serve as a reference for comparison. Results for the other five active motion models are presented in the Supplementary Note 4.

https://doi.org/10.1038/s41467-026-73626-8

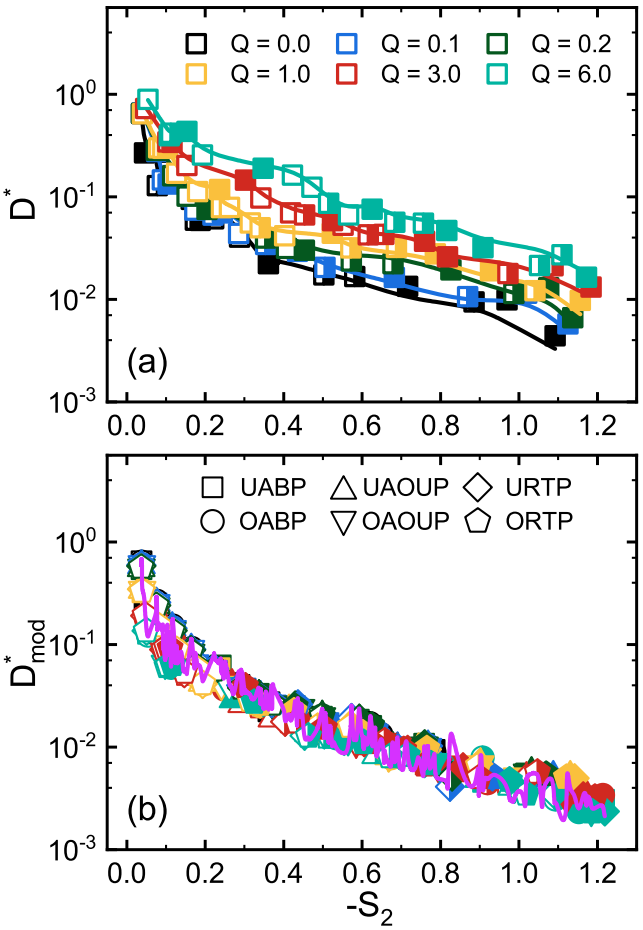

Fig. 4 | Universality of diffusion-structure scaling across diverse active models. **a** Simulation results for $D^* = D\Gamma^{-1}d_t^{-2}$ plotted as a function of S_2 for passive and active tracers in the UABP model, in both disordered and ordered backgrounds. Solid lines indicate fits to the original scaling relation (Eq. (4)). Different symbols denote tracers with different activity strength Q ranging from 0 to 6.0. **b** The same data replotted using the activity-modified normalization $D^*_{mod} = D\left[\Gamma(1+Q)d_t^2\right]^{-1}$, together with results from five additional active-motion models over the same range of Q. All data collapse onto a single master curve, the solid violet line denotes the fit to Eq. (5), demonstrating a unified scaling across passive and active tracers as well as diverse microscopic reorientation dynamics. Open, half-filled, and solid symbols correspond to disordered, square-lattice, and hexagonal-lattice backgrounds, respectively. Source data are provided as a Source Data file.

Remarkably, when the same data are replotted using the modified normalization in Fig. 4(b), all simulation results (across reorientation mechanisms, damping regimes, and matrix structures) collapse onto a single universal curve, in excellent agreement with the modified scaling relation, Eq. (5), with a single parameter $A = 8$ independent of active models. The larger fitting parameter compared to the experimental value can be attributed to the fact that in macroscopic granular experiments, the Einstein relationship is assumed, while particle-obstacle collisions are inelastic, and the noise is athermal. This demonstrates that the long-time diffusion of active tracers in complex media is controlled by the two-body structural entropy S_2 and the dimensionless persistence length $Q = v_d\tau_r/d_t$, which quantifies tracer activity, independent of the underlying stochastic process.

Discussion

Our work identifies a diffusion-structure relation for long-time normal diffusion of active tracers in complex media by incorporating directional persistence into a theoretical framework previously applicable only to passive systems. The transport is characterized by two key quantities: the structural entropy S_2 and the dimensionless persistence length $Q = v_d\tau_r/d_t$. This scaling provides a quantitative link between microscopic structure and macroscopic transport. Importantly, the observed scaling arises from long-time dynamics and is robust to microscopic details of interactions and reorientation dynamics, as demonstrated across experiments and multiple active-particle models. This theoretical framework highlights the key role of directional persistence in active diffusion within complex environments away from the dense ergodic-breaking regime, while intrinsically non-diffusive states lie beyond its scope.

The newly established scaling relation opens several promising directions for future research, including tests of its applicability in thermal systems such as colloidal suspensions, comparisons of fitted parameters between thermal and athermal environments, and systematic investigations of how hydrodynamic interactions affect the scaling behavior. Extending this framework to living active systems, such as motile bacteria and ciliated microorganisms, may further bridge nonequilibrium statistical physics and biological transport processes.

Methods

Experiment

As shown in Fig. 1(a), fixed polymethyl methacrylate (PMMA) cylinders with diameter d_l = 1 cm and height h = 2 cm served as immobile obstacles, arranged in three types of backgrounds: disordered configurations with obstacle number densities 0.005-0.025 cm^{-2}, and square and hexagonal lattices with lattice constants L = 3-8 cm. Disordered backgrounds were generated using a random placement algorithm with a minimum inter-obstacle separation exceeding 2 cm, ensuring that tracers move freely through the obstacle-obstacle gaps. Distinct disordered backgrounds were obtained by varying the obstacle number density. Vertical vibrations were applied with a magnitude of $Z = \zeta\sin(2\pi ft)$ and frequency f = 80 Hz. The dimensionless acceleration $\tilde{\Gamma}_{vib} = \zeta(2\pi f)^2/g = 3.0$, with g the gravitational acceleration, maintaining stable quasi-2D dynamics.

Tracers with diameter d_t = 1.5 cm were 3D-printed from polylactide, equipped with either symmetric (passive) or asymmetric (active) legs [inset, Fig. 1(a)][51,52]. For active tracers, the asymmetric leg geometry rectifies vertical vibrations into persistent horizontal motion. Propulsion speeds v_d = 2.04, 2.72, 3.40, and 4.08 cm/s were tuned via the leg inclination angle[68]. Images of the samples were recorded for 12-15 min at 100 frames/s under both obstacle-free and obstacle-present conditions in each measurement. For each tracer activity, more than 30 independent measurements were performed across disorder, square-lattice and hexagonal-lattice backgrounds. In total, over 160 experimental measurements were conducted for five tracer activities, yielding independent estimates of the long-time diffusion coefficient D and the corresponding two-body structural entropy S_2. Particle trajectories were extracted using particle tracking techniques[69], excluding regions within 1/8 of the vessel diameter to avoid boundary effects. All physical quantities reported, including diffusion coefficients and structural entropies, were evaluated only after the system was confirmed to have reached a steady state [Supplementary Note 5].

Simulation

Numerical simulations were performed in a 2D periodic box containing 1600 immobile matrix particles arranged in disordered, square, and hexagonal configurations, matching the experiments. Under the standard reduced simulation units, the matrix particle radius, tracer mass, and thermal energy k_BT are taken as the units of length, mass, and energy, respectively. The tracer diameter is set to $d_t = 0.25d_l$ (the matrix-particle diameter $d_l = 2.0$) in all models. To examine tracer-size dependence, we systematically varied the tracer-to-matrix size ratio $R = d_t/d_l$ in the OABP model (R = 0.25, 0.5, 0.75, 1.0, 1.25, and 1.5) while keeping d_l fixed. The corresponding results [Supplementary Note 6]

show that the fitting parameter A remains unchanged for all R, demonstrating that the proposed scaling relation is independent of tracer size, further confirming its universality. Tracer-matrix interactions were modeled using a truncated and shifted purely repulsive generalized Lennard-Jones potential, corresponding to a Weeks-Chandler-Andersen (WCA)-type interaction[70], $U(r) = 4\epsilon\left[\left(\frac{\sigma}{r}\right)^{2n} - \left(\frac{\sigma}{r}\right)^{n}\right] + \epsilon, \quad r < 2^{1/n}\sigma$, with interaction diameter $\sigma = (d_t + d_l)/2$, interaction strength $\epsilon = k_B T = 1.0$, and stiffness parameter $n = 12$. To verify robustness, additional simulations of the OABP model were performed using the same generalized form with $n = 6$ [Supplementary Note 7], which corresponds to the standard 12-6 WCA potential. Matrix packing fractions were varied to access a wide range of structural entropies. Translational and rotational thermal noises were included as independent Gaussian-distributed forces and torques following the fluctuation-dissipation relation. The persistence length $v_d\tau_r/d_t$ reached up to 6, significantly exceeding the experimental maximum of 1.9 limited by vibrational constraints.

We simulate active tracers under both underdamped and overdamped conditions using three representative models: active Brownian particles (ABPs)[33,53], run-and-tumble particles (RTPs)[54,55], and active Ornstein-Uhlenbeck particles (AOUPs)[56,57].

For ABPs, the translational dynamics depend on the damping regime. In the underdamped case, tracer motion obeys the Langevin equation,

$$m\dot{\boldsymbol{v}} = \mathbf{F}_r + \mathbf{F}_d + \mathbf{F}_G - \gamma\boldsymbol{v}, \tag{6}$$

where $m = 1$ is the tracer mass, $\gamma = 100$ is the translational friction coefficient, $\mathbf{F}_r$ is the tracer-matrix interaction force, $\mathbf{F}_d = \gamma\boldsymbol{v}_d$ is the self-propelling force, and $\mathbf{F}_G$ is a Gaussian stochastic force satisfying $\langle \mathbf{F}_G \rangle = 0$ and $\left\langle \mathrm{F}_G^{\alpha}(t)\mathrm{F}_G^{\beta}(t') \right\rangle = 2k_{\mathrm{B}}T\gamma\delta_{\alpha\beta}\delta(t-t')$. The propulsion speed is given by $\boldsymbol{v}_d = v_d\cos\theta\hat{\boldsymbol{e}}_x + v_d\sin\theta\hat{\boldsymbol{e}}_y$, where θ is the orientation angle, $\hat{\boldsymbol{e}}_x$ and $\hat{\boldsymbol{e}}_y$ are the unit vectors along the x and y directions, respectively. The rotational dynamics are governed by $I\ddot{\theta} = T_G^{\theta} - \gamma_r\dot{\theta}$, with moment of inertia $I = \frac{1}{8}md_t^2$, the rotational friction coefficient γ_r, and Gaussian stochastic torque T_G^{θ} satisfying $\left\langle T_G^{\theta}(t) \right\rangle = 0$ and $\left\langle T_G^{\theta}(t)T_G^{\theta}(t') \right\rangle = 2k_{\mathrm{B}}T\gamma_r\delta(t-t')$. In the overdamped case, the equations reduce to $\gamma\boldsymbol{v} = \mathbf{F}_r + \mathbf{F}_d + \mathbf{F}_G$ and $\gamma_r\dot{\theta} = T_G^{\theta}$. The rotational relaxation time is defined as $\tau_r = \gamma_r/(k_BT)$ and is tuned by varying γ_r.

For RTPs, the translational dynamics are identical to those of ABPs, but particles undergo instantaneous random tumbles, with orientations reset at an average time interval τ_r. For AOUPs, the translational dynamics are the same as for ABPs in both underdamped and overdamped conditions, while the self-propulsion speed $\boldsymbol{v}_d$ evolves according to an Ornstein-Uhlenbeck processes, $\tau_r\dot{\boldsymbol{v}}_d = -\boldsymbol{v}_d + \sqrt{2C}\boldsymbol{\eta}$, where C is the noise strength, and $\boldsymbol{\eta}$ denotes Gaussian white noise.

Simulations were performed with a time step $\Delta t = 10^{-3} \times d_l\sqrt{m/\epsilon}$. Each data point was averaged over eight independent trajectories, with 5×10^5 steps to relax the initialized system followed by 1.2×10^9 steps for data collection. For each active-motion model (OABP, ORTP, OAOUP, UABP, URTP, and UAOUP), more than 70 independent data points were obtained across different backgrounds, yielding over 440 simulation data points in total.

Data availability

The data supporting the findings of this study are available in the main text and Supplementary Information. Supplementary Movie 1 (passive) and Supplementary Movie 2 (active) are provided as Supplemental Material, and the data underlying the figures are available in the Source Data. Further information is available from the corresponding author upon request. Source data are provided with this paper.

Code availability

The Brownian dynamics simulation source code that was used to generate all simulation data for this study is included as Supplementary Data.

References

1. Zhang, H. P., Be'er, A., Florin, E. L. & Swinney, H. L. Collective motion and density fluctuations in bacterial colonies. *Proc. Natl. Acad. Sci. USA*. **107**, 13626–13630 (2010).
2. Theurkauff, I., Cottin-Bizonne, C., Palacci, J., Ybert, C. & Bocquet, L. Dynamic clustering in active colloidal suspensions with chemical signaling. *Phys. Rev. Lett.* **108**, 268303 (2012).
3. Buttinoni, I. et al. Dynamical clustering and phase separation in suspensions of self-propelled colloidal particles. *Phys. Rev. Lett.* **110**, 238301 (2013).
4. Noji, H., Yasuda, R., Yoshida, M. & Kinosita Jr, K. Direct observation of the rotation of F1-ATPase. *Nat. (Lond.)* **386**, 299–302 (1997).
5. Maggi, C., Saglimbeni, F., Dipalo, M., De Angelis, F. & Di Leonardo, R. Micromotors with asymmetric shape that efficiently convert light into work by thermocapillary effects. *Nat. Commun.* **6**, 7855 (2015).
6. Wang, S. & Wolynes, P. G. Active contractility in actomyosin networks. *Proc. Natl. Acad. Sci. USA*. **109**, 6446–6451 (2012).
7. Linsmeier, I. et al. Disordered actomyosin networks are sufficient to produce cooperative and telescopic contractility. *Nat. Commun.* **7**, 12615 (2016).
8. Qin, H., Wu, X., Xue, X. & Liu, H. Light actuated swarming and breathing-like motion of graphene oxide colloidal particles. *Commun. Chem.* **1**, 72 (2018).
9. Göth, N., Baul, U. & Dzubiella, J. Active responsive colloids driven by intrinsic dichotomous noise. *Phys. Rev. E* **106**, 064611 (2022).
10. Hallatschek, O. et al. Proliferating active matter. *Nat. Rev. Phys.* **5**, 407–419 (2023).
11. Weady, S. et al. Mechanics and morphology of proliferating cell collectives with self-inhibiting growth. *Phys. Rev. Lett.* **133**, 158402 (2024).
12. Liu, S., Shankar, S., Marchetti, M. C. & Wu, Y. Viscoelastic control of spatiotemporal order in bacterial active matter. *Nat. (Lond.)* **590**, 80–84 (2021).
13. Li, H., Chaté, H., Sano, M., Shi, X. Q. & Zhang, H. P. Robust edge flows in swarming bacterial colonies. *Phys. Rev. X* **14**, 041006 (2024).
14. Machemer, H. Ciliary activity and the origin of metachrony in Paramecium: effects of increased viscosity. *J. Exp. Biol.* **57**, 239–259 (1972).
15. Blake, J. R. & Sleigh, M. A. Mechanics of ciliary locomotion. *Biol. Rev. Camb. Philos. Soc.* **49**, 85–125 (1974).
16. Woolley, D. M. Motility of spermatozoa at surfaces. *Reproduction* **126**, 259–270 (2003).
17. Riedel, I. H., Kruse, K. & Howard, J. A self-organized vortex array of hydrodynamically entrained sperm cells. *Science* **309**, 300–303 (2005).
18. Lauga, E. & Goldstein, R. E. Dance of the microswimmers. *Phys. Today* **65**, 30–35 (2012).
19. Elgeti, J., Winkler, R. G. & Gompper, G. Physics of microswimmers—single particle motion and collective behavior: a review. *Rep. Prog. Phys.* **78**, 056601 (2015).
20. Lyu, X. et al. Active synthetic microrotors: Design strategies and applications. *ACS Nano* **17**, 11969–11993 (2023).
21. Wu, H. et al. High-performance Marangoni hydrogel rotors with asymmetric porosity and drag reduction profile. *Nat. Commun.* **14**, 20 (2023).
22. Zong, Y. et al. An optically driven bistable Janus rotor with patterned metal coatings. *ACS Nano* **9**, 10844–10851 (2015).

23. Tkachenko, G., Truong, V. G., Esporlas, C. L., Sanskriti, I. & Nic Chormaic, S. Evanescent field trapping and propulsion of Janus particles along optical nanofibers. *Nat. Commun.* **14**, 1691 (2023).
24. Zhang, J., Alert, R., Yan, J., Wingreen, N. S. & Granick, S. Active phase separation by turning towards regions of higher density. *Nat. Phys.* **17**, 961–967 (2021).
25. Ceron, S., Gardi, G., Petersen, K. & Sitti, M. Programmable self-organization of heterogeneous microrobot collectives. *Proc. Natl. Acad. Sci. USA.* **120**, e2221913120 (2023).
26. Janiak, J., Li, Y., Ferry, Y., Doinikov, A. A. & Ahmed, D. Acoustic microbubble propulsion, train-like assembly and cargo transport. *Nat. Commun.* **14**, 4705 (2023).
27. Surappa, S. et al. Dynamically reconfigurable acoustofluidic metasurface for subwavelength particle manipulation and assembly. *Nat. Commun.* **16**, 494 (2025).
28. Nelson, B. J., Kaliakatsos, I. K. & Abbott, J. J. Microrobots for minimally invasive medicine. *Annu. Rev. Biomed. Eng.* **12**, 55–85 (2010).
29. Patra, D. et al. Intelligent, self-powered, drug delivery systems. *Nanoscale* **5**, 1273–1283 (2013).
30. Abdelmohsen, L. K. E. A., Peng, F., Tu, Y. & Wilson, D. A. Micro- and nano-motors for biomedical applications. *J. Mater. Chem. B* **2**, 2395–2408 (2014).
31. Marchetti, M. C. et al. Hydrodynamics of soft active matter. *Rev. Mod. Phys.* **85**, 1143–1189 (2013).
32. Bechinger, C. et al. Active particles in complex and crowded environments. *Rev. Mod. Phys.* **88**, 045006 (2016).
33. Howse, J. R. et al. Self-motile colloidal particles: from directed propulsion to random walk. *Phys. Rev. Lett.* **99**, 048102 (2007).
34. Golestanian, R. Anomalous diffusion of symmetric and asymmetric active colloids. *Phys. Rev. Lett.* **102**, 188305 (2009).
35. Martens, K., Angelani, L., Di Leonardo, R. & Bocquet, L. Probability distributions for the run-and-tumble bacterial dynamics: An analogy to the Lorentz model. *Eur. Phys. J. E* **35**, 1–6 (2012).
36. Bricard, A., Caussin, J.-B., Desreumaux, N., Dauchot, O. & Bartolo, D. Emergence of macroscopic directed motion in populations of motile colloids. *Nat. (Lond.)* **503**, 95–98 (2013).
37. Bhattacharjee, T. & Datta, S. S. Bacterial hopping and trapping in porous media. *Nat. Commun.* **10**, 2075 (2019).
38. Granek, O. et al. Colloquium: Inclusions, boundaries, and disorder in scalar active matter. *Rev. Mod. Phys.* **96**, 031003 (2024).
39. Chepizhko, O. & Peruani, F. Diffusion, subdiffusion, and trapping of active particles in heterogeneous media. *Phys. Rev. Lett.* **111**, 160604 (2013).
40. Sipos, O., Nagy, K., Di Leonardo, R. & Galajda, P. Hydrodynamic trapping of swimming bacteria by convex walls. *Phys. Rev. Lett.* **114**, 258104 (2015).
41. Paoluzzi, M., Di Leonardo, R. & Angelani, L. Run-and-tumble particles in speckle fields. *J. Phys.: Condens. Matter* **26**, 375101 (2014).
42. Pesce, G. et al. Step-by-step guide to the realization of advanced optical tweezers. *J. Opt. Soc. Am. B* **32**, B84–B98 (2015).
43. Nourhani, A., Crespi, V. H. & Lammert, P. E. Guiding chiral self-propellers in a periodic potential. *Phys. Rev. Lett.* **115**, 118101 (2015).
44. Chan, C. W. et al. Chiral active particles are sensitive reporters to environmental geometry. *Nat. Commun.* **15**, 1406 (2024).
45. Dzugutov, M. A universal scaling law for atomic diffusion in condensed matter. *Nat. (Lond.)* **381**, 137 (1996).
46. Rosenfeld, Y. A quasi-universal scaling law for atomic transport in simple fluids. *J. Phys.: Condens. Matter* **11**, 5415–5427 (1999).
47. Samanta, A., Ali, S. M. & Ghosh, S. K. New universal scaling laws of diffusion and kolmogorov-sinai entropy in simple liquids. *Phys. Rev. Lett.* **92**, 145901–146100 (2004).
48. Ning, L. et al. Universal scaling law for colloidal diffusion in complex media. *Phys. Rev. Lett.* **122**, 178002 (2019).
49. Ning, L., Liu, P., Ye, F., Yang, M. & Chen, K. Diffusion of colloidal particles in model porous media. *Phys. Rev. E* **103**, 022608 (2021).
50. Sachin, C. & Joy, A. Entropy scaling laws in self propelled glass formers. *Phys. A* **588**, 126578 (2022).
51. Scholz, C. & Pöschel, T. Velocity distribution of a homogeneously driven two-dimensional granular gas. *Phys. Rev. Lett.* **118**, 198003 (2017).
52. Scholz, C., Engel, M. & Pöschel, T. Rotating robots move collectively and self-organize. *Nat. Commun.* **9**, 931 (2018).
53. Liu, P., Ye, S., Ye, F., Chen, K. & Yang, M. Constraint dependence of active depletion forces on passive particles. *Phys. Rev. Lett.* **124**, 158001 (2020).
54. Berg, H. C. & Turner, L. Movement of microorganisms in viscous environments. *Nat. (Lond.)* **278**, 349–351 (1979).
55. Tailleur, J. & Cates, M. E. Statistical mechanics of interacting run-and-tumble bacteria. *Phys. Rev. Lett.* **100**, 218103 (2008).
56. Uhlenbeck, G. E. & Ornstein, L. S. On the theory of the brownian motion. *Phys. Rev.* **36**, 823 (1930).
57. Fodor, É. et al. How far from equilibrium is active matter? *Phys. Rev. Lett.* **117**, 038103 (2016).
58. Ma, X. et al. Test of the universal scaling law of diffusion in colloidal monolayers. *Phys. Rev. Lett.* **110**, 078302 (2013).
59. Caprini, L. & Löwen, H. Flocking without alignment interactions in attractive active brownian particles. *Phys. Rev. Lett.* **130**, 148202 (2023).
60. Baranyai, A. & Evans, D. J. Direct entropy calculation from computer simulation of liquids. *Phys. Rev. A* **40**, 3817–3822 (1989).
61. Wang, C.-H., Yu, S.-H. & Chen, P. Universal scaling laws of diffusion in two-dimensional granular liquids. *Phys. Rev. E* **91**, 060201 (2015).
62. McNamara, S. & Luding, S. Energy flows in vibrated granular media. *Phys. Rev. E* **58**, 813 (1998).
63. Tatsumi, S., Murayama, Y., Hayakawa, H. & Sano, M. Experimental study on the kinetics of granular gases under microgravity. *J. Fluid Mech.* **641**, 521–539 (2009).
64. Longuet-Higgins, H. C. & Pople, J. A. Transport properties of a dense fluid of hard spheres. *J. Chem. Phys.* **25**, 884–889 (1956).
65. Srivastava, R. & Khanna, K. N. Stokes-Einstein relation in two- and three-dimensional fluids. *J. Chem. Eng. Data* **54**, 1452–1456 (2009).
66. Makse, H. A. & Kurchan, J. Testing the thermodynamic approach to granular matter with a numerical model of a decisive experiment. *Nat. (Lond.)* **415**, 614–617 (2002).
67. Zeng, Z. et al. Equivalence of fluctuation-dissipation and Edwards' temperature in cyclically sheared granular systems. *Phys. Rev. Lett.* **129**, 228004 (2022).
68. Koumakis, N., Gnoli, A., Maggi, C., Puglisi, A. & Leonardo, R. D. Mechanism of self-propulsion in 3D-printed active granular particles. *N. J. Phys.* **18**, 113046 (2016).
69. Ning, L. et al. Hydrodynamics-induced long-range attraction between plates in bacterial suspensions. *Phys. Rev. Lett.* **131**, 158301 (2023).
70. Weeks, J. D., Chandler, D. & Andersen, H. C. Role of repulsive forces in determining the equilibrium structure of simple liquids. *J. Chem. Phys.* **54**, 5237–5247 (1971).

Acknowledgements

The authors thank the reviewers for their constructive comments and suggestions.

Author contributions

P.L., M.Y., R.N., L.N., and N.Z. conceived the research. P.L., M.Y., L.N., and N.Z. designed the experimental setup. Q.Z., X.Z., and H.Z. performed and analyzed the experiments. P.L. and Y.T. developed the simulation code. Y.T. and X.Y. performed and analyzed the simulations. All authors discussed the results and wrote the manuscript.

Funding
This work was supported by the National Natural Science Foundation of China (Grants No. 12374205, No. 12304245, No. T2325027, No. 12274448, and No. 12475031), the Shandong Provincial Natural Science Foundation (Grant No. ZR2024YQ017), the Beijing National Laboratory for Condensed Matter Physics (Grant No. 2024BNLCMPKF009), the Science Foundation of China University of Petroleum, Beijing (Grants No. 2462024BJRC010 and No. 2462023YJRC031), the Beijing Institute of Technology Research Fund Program for Young Scholars, the Academic Research Fund from the Singapore Ministry of Education (RG151/23, and RG88/25), and the National Research Foundation, Singapore, under its 29th Competitive Research Program (CRP) Call (NRF-CRP29-2022-0002).

Competing interests
The authors declare no competing interests.

Additional information
Supplementary information The online version contains supplementary material available at https://doi.org/10.1038/s41467-026-73626-8.

Correspondence and requests for materials should be addressed to Ning Zheng, Luhui Ning, Ran Ni, Mingcheng Yang or Peng Liu.

Peer review information *Nature Communications* thanks Sam Cameron, Benoit Mahault, Theo Spornhauer, and the other, anonymous, reviewer for their contribution to the peer review of this work. A peer review file is available.